RSC Advances

PAPER

View Article Online
View Journal | View Issue

Cite this: *RSC Adv.*, 2023, **13**, 30151

Synthesis and characterization of Mg-hydroxyapatite and its cellulose hybridized structure as enhanced bio-carrier of oxaliplatin drug; equilibrium and release kinetics

Alaa T. Okasha,[ab] Ahmed A. Abdel-Khalek,[b] Hassan Ahmed Rudayni,[c] Wail Al Zoubi,[d] Haifa E. Alfassam,[e] Ahmed A. Allam[f] and Mostafa R. Abukhadra *[ag]

An advanced form of magnesium-doped hydroxyapatite (Mg HAP) was synthesized and hybridized with cellulose fibers, producing a safe biocomposite (CF/Mg HAP) as an enhanced delivery structure of traditional oxaliplatin (OXPN) chemotherapy drug during the treatment stages of colorectal cancer. The qualifications of CF/Mg HAP as a carrier for OXPN were followed based on loading, release, and cytotoxicity as compared to Mg HAP. The CF/Mg HAP composite exhibits a notably higher OXPN encapsulation capacity (256.2 mg g^{-1}) than the Mg HAP phase (148.9 mg g^{-1}). The OXPN encapsulation process into CF/Mg HAP displays the isotherm behavior of the Langmuir model (R^2 = 0.99) and the kinetic assumptions of pseudo-first-order kinetics (R^2 > 0.95). The steric studies reflect a strong increment in the quantities of the free sites after the cellulose hybridization steps (Nm = 178.58 mg g^{-1}) as compared to pure Mg HAP (Nm = 69.39 mg g^{-1}). Also, the capacity of each site was enhanced to be loaded by 2 OXPN molecules (n = 1.43) in a vertical orientation. The OXPN encapsulation energy into CF/Mg HAP (<40 kJ mol^{-1}) reflects physical encapsulation reactions involving van der Waals forces and hydrogen bonding. The OXPN release profiles of CF/Mg HAP exhibit slow and controlled properties for about 100 h, either at pH 5.5 or pH 7.4. The release kinetics and diffusion exponent (>0.45) signify non-Fickian transport and a complex erosion/diffusion release mechanism. The free CF/Mg HAP particles display a considerable cytotoxic effect on the HCT-116 cancer cells (21.82% cell viability), and their OXPN-loaded product shows a strong cytotoxic effect (1.85% cell viability).

Received 26th June 2023
Accepted 28th September 2023

DOI: 10.1039/d3ra04268e

rsc.li/rsc-advances

1. Introduction

Non-contagious diseases, particularly cancer, are responsible for roughly 72% of all recorded deaths worldwide, which is expected to rise to 75% within the next few years.[1,2] Colorectal cancer is a common malignant type of cancer that affects approximately 13% of cancer patients worldwide and represents one of the two major factors causing death and increasing the global death rate.[3–5] Colorectal cancer begins as a polyp within the mucosal layers and then spreads to the current submucosa and adjacent tissues. In the advanced stages of colorectal cancer, the newly formed neoplastic cells spread to other nearby organs and lymph nodes.[6] Therefore, the production of effective and safe therapies that can significantly inhibit the tumor cells of colorectal cancer without detectable strong side effects represents a critical issue and a hot research point for the international health authorities and the scientific communities.[5,7]

Various types of chemotherapies drugs are widely used to conquer the continuous and progressive growth of cancer cells such as 5-fluorouracil, oxaliplatin, cisplatin, cyclophosphamide, and altretamine.[8,9] The most common chemotherapies drugs work by causing a lot of oxidative stress and stopping DNA replication, which kills the infected cancer cells.[5,10] Regrettably, the majorities of the commonly used chemotherapies drugs have toxic effects on normal cells and cause many serious side effects such as nausea, renal damage, and bone marrow suppression, especially with increasing the applied dosages.[11,12] Therefore, several studies have been established to

[a]*Materials Technologies and their Applications Lab, Geology Department, Faculty of Science, Beni-Suef University, Beni Suef, Egypt. E-mail: Abukhadra89@Science.bsu.edu.eg*

[b]*Department of Chemistry, Faculty of Science, Beni-Suef University, 62514 Beni-Suef, Egypt*

[c]*Department of Biology, College of Science, Imam Muhammad Ibn Saud Islamic University, Riyadh 11623, Saudi Arabia*

[d]*Materials Electrochemistry Laboratory, School of Materials Science and Engineering, Yeungnam University, Gyeongsan 38541, Republic of Korea*

[e]*Princess Nourah Bint Abdulrahman University, College of Science, Biology Department, Riyadh, Saudi Arabia*

[f]*Zoology Department, Faculty of Science, Beni-Suef University, Beni-Suef, Egypt*

[g]*Geology Department, Faculty of Science, Beni-Suef University, Beni-Suef, Egypt*

enhance the safety, biocompatibility, therapeutic influences, and selectivity of the known species of traditional chemotherapies drugs.[1] This enhancement was suggested to be performed either by the production of innovative new types of anticancer therapies or by inducing the activity and biosafety of the commercially used traditional types.[3,13]

Oxaliplatin (OXPL) is a drug that is often used in chemotherapy drug to treat cancer cells that have spread to other parts of the body. This is because it can form reactive species of platinum complexes that stop cancer cells from copying their DNA.[3,10,11] However, the FAD organization approved of its use as a highly effective anticancer drug.[5,6] But the chemical structure of OXPN isn't very soluble in human blood, and its metabolites are very bad for normal tissues. This makes its use and dosages very limited.[5,14,15] Also, the OXPN drug was said to have serious side effects like problems with the GI tract, nausea, digestive problems, cardiotoxicity, neurotoxicity, and myelotoxicity.[8,10,14] Because of this, researchers looked at a number of advanced delivery systems as possible ways to improve the therapeutic activity, solubility, and selectivity of OXPN.[5,15] Recent studies of carriers show that they improve OXPN's solubility, therapeutic effectiveness, curative value, and rate of release.[9,15,16] The effective encapsulation of the OXPN molecules into advanced biocompatible carriers was strongly recommended to regulate the delivered dosages along certain intervals and at controlled rates to avoid the commonly reported health drawbacks and expand the interaction duration.[9,15]

In this regard, several inorganic, organic, and hybrid organic/inorganic structures such as mesoporous silica, alginate nanogels, polymers, liposomes, bentonite/cellulose composites, lipid nanoparticles, and hydroxyapatite particles were evaluated as promising drug carriers for chemotherapies drugs. The previous materials demonstrated a significant effect on inducing the permeability and retention properties of the drug.[5,6,9,15,17] Hydroxyapatite is a promising biomaterial species of the apatite family that exhibits $Ca_{10}(PO_4)_6(OH)_2$ and is widely used in numerous medical industries, including tissue and bone engineering as well as effective drug delivery structures.[18–21] This was assigned to its significant chemical stability, surface area, acid–base adjustability, ion exchange capacity, long shelf life, flexible structure, and adsorption capacity.[22–24] As a biomaterial, it possesses bioactive, biodegradable, biocompatible, and osteoconductive characteristics without generating inflammation or toxicity.[19,25] However, the hydrophilic properties of its structure reduce its efficiency as a carrier of common drugs that have an organic chemical structure.[22,26] Consequently, several studies have been developed to enhance the physical, chemical, and biological properties of HAP by controlling its morphology, chemical composition, and crystallite size, in addition to its surface functionalization and hybridization by polymers and other active chemical groups.[22,27–29] The hybrid composites of HAP and reactive natural or synthetic polymers can successfully overcome the reported drawbacks during the application of them as delivery systems, including the low encapsulation capacity, uncontrollable release rate, high brittleness, easy agglomeration, and poor plasticity.[21,30]

Therefore, the objective of the current study is to synthesize a hybrid structure of cellulose/Mg-hydroxyapatite (CF/Mg HAP) with enhanced physicochemical, biocompatible, and anticancer properties while evaluating it as a low-cost and efficient delivery system of oxaliplatin (OXPN). The cellulose fibers were selected as functionalized polysaccharide biopolymers for their availability as a natural-based product that is characterized by significant surface reactivity, non-toxicity, thermal stability, biodegradability, chemical stability, and biocompatibility.[31–33] For the first time, the encapsulation behaviors, release profiles, and cytotoxic effects on colorectal cancer cells (HCT-116) of Mg HAP and its cellulose-functionalized derivative CF/Mg HAP as potential delivery structures of OXPN molecules were evaluated in depth in this study. Furthermore, kinetic and equilibrium investigations were used to depict the mechanisms that affect the encapsulation and release processes.

2. Experimental work

2.1. Materials

The phosphorite precursors (P_2O_5 (28 wt%), CaO (46 wt%), Fe_2O_3 (2 wt%), SiO_2 (12 wt%), Al_2O_3 (0.8 wt%), F (2.8 wt%), Na_2O (4 wt%), MgO (0.5 wt%), and LOI (7 wt%)) were delivered from the Quseir area, Red Sea, Egypt. Magnesium nitrate hexahydrate (99% purity; Sigma-Aldrich, Egypt) was applied as the doped magnesium ions. Nitric acid (40% purity; Sigma-Aldrich, Egypt) and ammonium hydroxide (25% NH_3; Sigma-Aldrich, Egypt) were used during the dissolving and precipitation steps. The cellulose fibers that were used during the functionalization reactions are microcrystalline cellulose of analytical grade (Sigma-Aldrich; Egypt) in addition to dimethyl sulfoxide (DMSO) (CAS 67-68-5; >99.5%; Sigma-Aldrich) as a dissolving reagent. Commercial Oxaliplatin drug with SP-4-2-[(1*R*-trans)]-(1,2-cyclohexanediamine-*N*,*N*′)-[ethanedioata(2-)-*O*,*O*′] platinum chemical structure and 397.29 MW were used to study the loading, release, and cytotoxic properties of the structures as delivery systems and were obtained from Sigma-Aldrich Company, Egypt.

2.2. Synthesis of magnesium hydroxyapatite (Mg HAP)

The fabrication of Mg HAP was accomplished based on the reported dissolution–precipitation method by Okasha *et al.*[34] The phosphorite raw samples were first ground to be within the size range of 25–150 μm. Then, the ground product (15 g) was dissolved completely in nitric acid (200 mL; 1 M) over 24 h at 343 K by a magnetic stirrer at an adjusted speed of 200 rpm. The residual solids of the silicate impurities were removed by filtration utilizing Whatman filter paper (40 μm) remaining solution of Ca^{2+} and PO_4^{3-} ions. Afterward, the magnesium nitrate salt (10 g) was dissolved within the filtered solution under stirring for 2 h. Then the ammonium solution (25% NH_3) was added to the mixture at a slow rate to ensure the successful precipitation of the white gel of Mg HAP. After that, the synthesis system was left at room temperature for 24 h, and then the Mg HAP product was extracted by another cycle of filtration. Finally, the synthetic Mg HAP particles were washed

for five runs and dried for 10 h at 373 K in an electric muffle furnace to be incorporated into the additional synthesis and application procedures.

2.3. Synthesis of cellulose functionalized magnesium hydroxyapatite (CF/Mg HAP)

The functionalization of the obtained Mg HAP product with the cellulose fibers was performed based on the reported method by Altoom *et al.*[11] 2 g of the prepared Mg HAP particles were homogenized within distilled water (50 mL) for 120 min using a complex mixing system that involves a magnetic stirrer (500 rpm) supplied with a sonication source (240 W). As a parallel process, 1 g of the cellulose fibers was dispersed within 50 mL of DMSO for 24 h by stirring at 500 rpm, and homogenization was induced after that by a sonication step for 120 min. The obtained cellulose suspension was added to the previously prepared Mg HAP suspension under continuous homogenization processes for 24 h using both a magnetic stirrer (500 rpm) and sonication irradiation (240 W). Then, the obtained CF/Mg HAP composite particles were extracted from the residual solution by centrifugation at 3500 rpm for 15 min, washed several times to neutralize the surface of the composite, and dried for 24 h at 60 °C.

2.4. Analytical techniques

The crystalline phases as well as the structural properties during the synthesis procedures were determined according to the X-ray diffraction patterns, which were obtained by a PANalytical-Empyrean X-ray diffractometer within the determination range from 0 up to 70°. The essential chemical groups as well as the integrated groups during the functionalization steps were identified according to the FT-IR spectra of the prepared structures using a Fourier Transform Infrared Spectrometer (FTIR-8400S; Shimadzu) within an estimation range of 400 cm^{-1} to 4000 cm^{-1}. The surficial morphologies and their changes in terms of the modification procedures were inspected based on the SEM images of the synthetic materials by scanning electron microscopy (Gemini, Zeiss Ultra 55). Texturally, the surface area and porosity properties were evaluated according to the obtained N_2 adsorption/desorption isotherm curves of the raw and prepared materials by a surface area analyzer (Beckman Coulter SA3100).

2.5. OXP encapsulation studies

The encapsulating studies of OXPN into both Mg HAP and CF/Mg HAP were evaluated based on the fundamentally investigated factors to control the OXPN encapsulated dosage in addition to the maximum encapsulation capacities. The assessed factors are the pH (2–9), encapsulation duration (1–24 h), OXPN concentration (100–800 mg L^{-1}), and temperature (20–50 °C). The Mg HAP and CF/Mg HAP particles were homogenized effectively within the prepared OXPN solutions (50 mL) using a vortex rotator. After the equilibration period of each encapsulation test, the Mg HAP and CF/Mg HAP particles were removed from the solutions by filtration utilizing Whatman filter paper, and the remaining OXPN concentrations in the solutions were measured by a UV-Vis spectrophotometer at a fixed determination wavelength (λ_{max} = 209 nm). The determined remaining OXPN concentrations were applied to calculate the encapsulation capacities of Mg HAP and CF/Mg HAP particles in mg g^{-1} according to eqn (1). The OXPN encapsulation tests into Mg HAP and CF/Mg HAP particles were accomplished in triplicate, and the estimated average values were presented in the studies with standard deviations of 3.8%.

$$\text{Capacity } (\text{mg g}^{-1}) = \frac{(\text{initial concentration} - \text{residual concentration}) \times \text{solvent volume}}{\text{carrier weight}} \quad (1)$$

2.6. The release studies

The OXPN release profiles of Mg HAP and CF/Mg HAP particles were evaluated within two types of chemical buffers (phosphate buffer (pH 7.4) and acetate buffer (pH 5.5)), considering the experimental temperature of 37.5 °C. The OXPN-encapsulated Mg HAP and CF/Mg HAP particles (100 mg g^{-1}) were carefully dispersed separately within 500 mL of the prepared chemical release buffers. The homogenization processes between the OXPN-loaded Mg HAP and CF/Mg HAP particles and the two buffers were accomplished by the DISTEK dissolution apparatus for 120 h at 200 rpm as the rotation speed of the vessels. Samples of the two buffers (5 mL) were regularly extracted from the bulk release solutions at specific time intervals to follow the percentages of the diffused OXPN molecules from the Mg HAP and CF/Mg HAP particles by a UV-Vis spectrophotometer at a fixed determination wavelength (λ_{max} = 209 nm). The regularly obtained samples during the release tests of OXPN from Mg HAP and CF/Mg HAP particles were re-added immediately after the measurements to the bulk release buffers to maintain the volume at the same values throughout the total investigated release period. The OXPN release tests into Mg HAP and CF/Mg HAP particles were accomplished in triplicate, and the estimated average values were presented in the studies considering eqn (2) to determine the release percentages with standard deviations <3.66%.

$$\text{OXPN release } (\%) = \frac{\text{the amount of released OXPN}}{\text{amount of loaded OXPN}} \times 100 \quad (2)$$

2.7. *In vitro* cytotoxicity

2.7.1. Cell lines. The anti-cancer and cytotoxicity properties of free Mg HAP and CF/Mg HAP particles and their OXPN loading samples were evaluated against fresh colorectal cells and colorectal cancer cells. The tests were conducted at the Regional Center for Microbiology & Biotechnology, Al-Azhar University, Egypt. The incorporated chemicals and reagents during the tests are Gentamycin, colorectal malignant cell lines (HCT-116) (American Type Culture Collection), 0.25% trypsin–EDTA, dimethyl sulfoxide (DMSO), RPMI-1640, DMEM, fetal

bovine serum, HEPES buffer, and 3-(4,5-dimethylthiazol-2-yl)-2.5 diphenyltetrazolium bromide (MTT 99%).

2.7.2. *In vitro* cytotoxicity. The cancer cell lines (HCT-116) were first carefully immersed within RPMI-1640 as the incorporated culturing medium at specific conditions of temperature (37 °C) and atmosphere of 5% of CO_2. Afterward, the incorporated culturing medium was significantly supplemented with gentamycin (50 μg mL^{-1}) in addition to fetal calf serum (10%). The previously reported procedures were carefully repeated three times per week, and then the HCT-116 cell lines (5×10^4 cell per well) were immersed for 24 h within specific Corning® 96-well plates. After that, the free Mg HAP and CF/Mg HAP particles and their OXPN loading samples were homogenized with the cell lines in a series of separate tests and incubated for 24 h. During this period, the generated viable cells were measured according to the criteria of the MTT cell proliferation assay. By the end of the incubation process (after 24 h), the previously incorporated culturing medium was removed and replaced immediately with a mixture of 100 μL of fresh RPMI medium and 10 μL of MTT (12 mM). This mixture was incubated for 5 h, and the purple formazan generated during this incubation was dissolved by DMSO (50 μL). The optical density of the treated HCT-116 cell lines, either by the free Mg HAP and CF/Mg HAP particles or their OXPN loading samples, was measured using a microplate at 590 nm as the measuring wavelength. The measured values were applied directly to calculate the cell viability percentage as in eqn (3).

$$\text{Cell viability } (\%) = \frac{\text{mean OD}}{\text{control OD}} \times 100 \quad (3)$$

3. Results and discussion

3.1. Characterization of the carrier

3.1.1. XRD analysis. The XRD patterns reflected the structural effect of the integration procedures on the individual components (Fig. 1). The recognized diffraction pattern of Mg HAP reflects the successful synthesis of hydroxyapatite with an average crystallite size of 11.8 nm. The identification peaks of Mg HAP were detected at 26.28°, 28.63°, 32.29°, 40°, 47.1°, 50.29°, 3.55°, and 64.28° (JCPSD 00-001-1008) (Fig. 1A). The remarkable upshifting of these peaks as compared to the reference pattern of hydroxyapatite was assigned to the structural impact of the doped Mg^{2+}.[28,35] The diffraction pattern of the hybridized cellulose fibers reveals its crystalline properties, with common peaks of commercial cellulose at 14.6° (1$\bar{1}$0), 16.62° (110), 22.7° (200), and 34.6° (004) (JCPDS card no. 00-056-1718) (Fig. 1B). The observed pattern of CF/Mg HAP demonstrates the existence of the diffraction peaks of hydroxyapatite (25.97°, 39.65°, and 49.66°) in addition to the hybridized cellulose (16.47° and 22.77°) but at notably deviated positions (Fig. 1C). This pattern demonstrates the hybridization and functionalization of Mg HAP with the cellulose chains, which might be involved in the grafting of the cellulose chains and/or the formation of chemical complexes or hydrogen bonding.

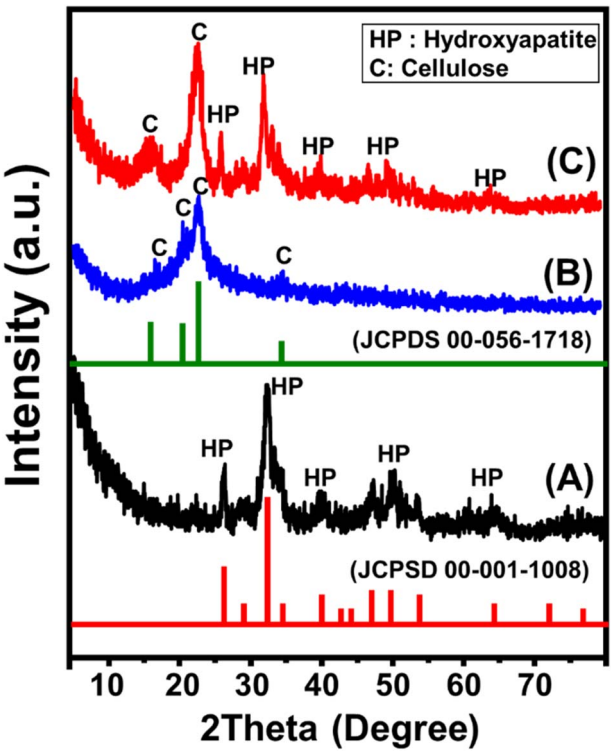

Fig. 1 XRD pattern of synthetic magnesium hydroxyapatite (Mg HAP) (A), cellulose fibers (B), and synthetic CF/Mg HAP (C).

3.1.2. SEM analysis. The synthetic Mg HAP was detected as needle-like structure that connected with each other, forming branches or bundles (Fig. 2A and B). The random orientation of the Mg HAP bundles in addition to their intersection as network or web structure resulted in a porous matrix in addition to the structural porosity of Mg HAP (Fig. 2B). The high SEM magnification image of the Mg HAP bundles revealed the decoration of the particles with numerous nano-dots (Fig. 2C). The synthetic Mg HAP bundles display a 20–60 nm average diameter and 50–250 nm average length. Whereas the individual particulates of the bundles exhibit an average diameter from 2 to 10 nm and an average length between 20 and >100 nm. Moreover, the EDX spectrum of the detected bundles reflected its composition as magnesium-rich hydroxyapatite (Ca, P, Mg, and O) (Fig. 2D). Regarding the observed SEM images of the synthetic CF/Mg HAP, the recognized particles reflected significant orientation of the prepared Mg HAP particles on the surface of the needle like particles of the cellulose fibers (Fig. 2E and F). This orientation gives the surface of cellulose an irregular and rugged topography, which increases the surface area. Moreover, such morphological properties enhance the exposure properties of the Mg HAP particles and reduce their agglomeration affinity, giving them a high interactive interface and more active sites during the encapsulation and release processes of the OXPN drug. Additionally, the textural properties reflected a significant effect of the described morphological features on the porosity and surface area of the composite. The determined surface area of Mg HAP (93.7 m^2 g^{-1}) is enhanced at a considerable rate after hybridization with cellulose to be 98.3 m^2 g^{-1}.

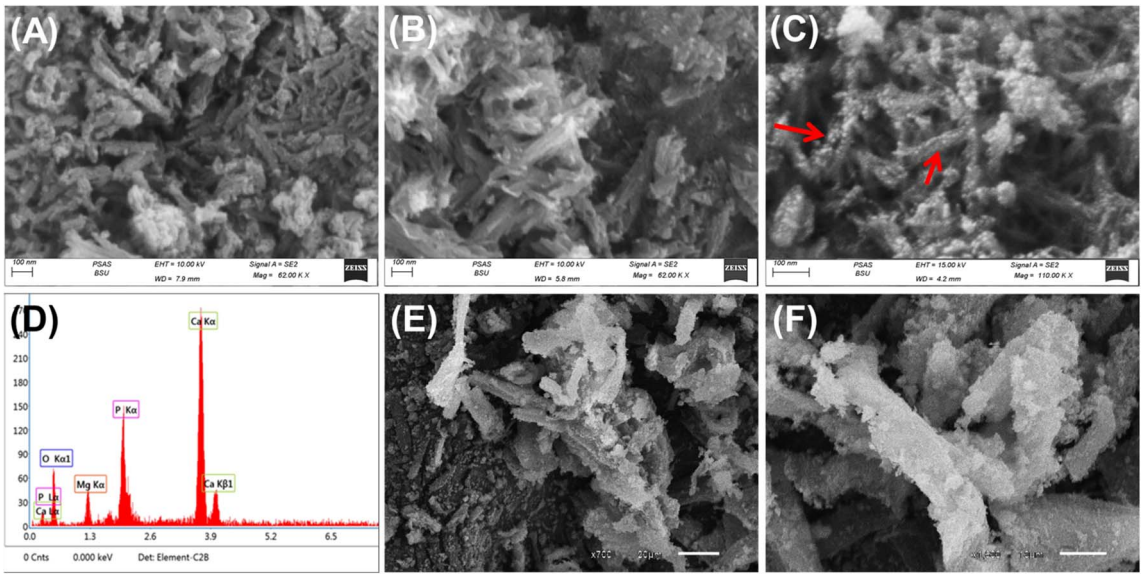

Fig. 2 SEM images of the synthetic magnesium hydroxyapatite (Mg HAP) (A–C), EDX spectrum of the synthetic Mg HAP (D), and SEM images of the synthetic CF/Mg HAP (E and F).

3.1.3. FT-IR analysis. The FT-IR spectra of Mg.HPA, cellulose fibers, CF/Mg HAP, and OXPN-encapsulated CF/Mg HAP were evaluated to follow the expected changes in the essential chemical groups during the functionalization procedures (Fig. 3). The essential functional groups of hydroxyapatite were clearly identified from the spectrum of Mg HAP (Fig. 3A). This involved the essential phosphorus bearing chemical groups such as asymmetric P–O bonds of the PO_4^{3-} group (1039.4 cm^{-1}), HPO_4^{2-} groups (871.2 cm^{-1}), symmetric (570.8 cm^{-1}) and asymmetric (603.3 cm^{-1}) O–P–O bonds of the PO_4^{3-} groups in addition to the hydroxyl groups (O–H) (3434.4 cm^{-1}) (Fig. 3A).[22,28,36,37] The corresponding bands of N–H bonds (1390.6 cm^{-1}) and CO_3^{2-} groups (2376.19 cm^{-1}) were assigned to the trapped ions during the dissolution of the precursor by nitric acid and the evolved CO_2 gas from the dissolved carbonate impurities, respectively (Fig. 3A).[34,38,39] The spectrum of separated cellulose fibers demonstrates clearly the bands of the structural organic groups such as –CH-bearing chemical groups (2914 and 1367 cm^{-1}), –C–O–C bonds within the pyranose rings (1057 cm^{-1}), and the β-glycosidic linkages (897 cm^{-1})[11,40] (Fig. 3B).

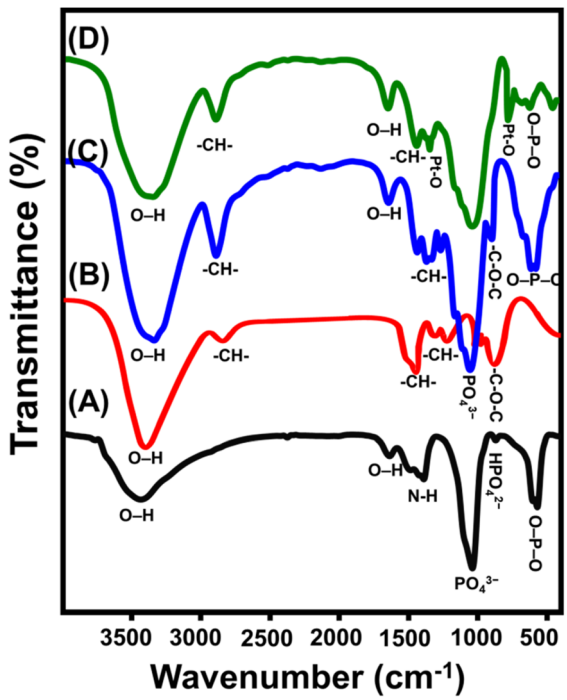

Fig. 3 FT-IR spectra of synthetic magnesium hydroxyapatite (Mg HAP) (A), integrated cellulose fibers (B), synthetic CF/Mg HAP (C), and OXPN loaded CF/Mg HAP (D).

The spectrum of the CF/Mg HAP composite involves the bands of the organic structure of cellulose as well as inorganic hydroxyapatite (Fig. 3C). The detected chemical groups of Mg HAP are 3352 cm^{-1} (OH stretching), 1048 cm^{-1} (P–O stretching vibration for PO_4^{3-}), and 573.78 (P–O bending vibration for PO_4^{3-}) (Fig. 3C). The identified chemical groups of cellulose that form the spectrum of the CF/Mg HAP composite are 2900.5 and 1369 cm^{-1} (–CH bearing groups) and 1048.5 cm^{-1} (–C–O–C of the pyranose ring) (Fig. 3C). The previously identified hybrid organic/inorganic chemical groups, in addition to the considerable fluctuation in the positions of their identification bands, validate the effective integration between cellulose and Mg HAP in composite and the considerable chemical interaction between their reactive functional groups. Regarding the spectrum of the OXPN-encapsulated CF/Mg HAP composite, there is observable shifting in the previously described bands of the present organic and inorganic chemical groups (Fig. 3D). Additionally, the appearance of two new bands related to the symmetric (828.7 cm^{-1}) and asymmetric (1290.4 cm^{-1}) stretching of Pt–O within the structure of the OXPN drug signify

the effective trapping and encapsulation of the drug molecules within the structure of the CF/Mg HAP composite[5,41,42] (Fig. 3D).

3.2. Encapsulation of OXPN drug

3.2.1. Influence of the encapsulation parameters

3.2.1.1. Effect of pH. The effect of the solution's pH on the achieved encapsulation capacities by both Mg HAP and CF/Mg HAP was followed within a tested range from pH 2 until pH 8 at adjusted values of the other affecting variables [OXPN concentration: 200 mg L^{-1}; dosage: 20 mg; temperature: 20 °C; duration: 6 h; volume: 50 mL]. The experimentally detected encapsulation of OXPN into Mg HAP and CF/Mg HAP exhibits remarkable enhancement when performing the tests at high pH conditions (Fig. 4A). This can be detected from pH 3 (Mg HAP (2.3 mg g^{-1}) and CF/Mg HAP (44.8 mg g^{-1})) until pH 8 (Mg HAP (26.8 mg g^{-1}) and CF/Mg HAP (96.2 mg g^{-1})) (Fig. 4A). Therefore, the encapsulation reactions at the basic pH values were recommended during the loading of OXPN into both Mg HAP and CF/Mg HAP. Generally, the solution's pH significantly influences the ionization behavior of OXPN, a dissolved chemical compound, as well as the dominant surficial charges of Mg HAP and CF/Mg HAP. Regarding OXPN, it is characterized by significant mobility and solubility in acidic conditions, which decreases its effective encapsulation properties.[11,16] Moreover, the dissolved OXPN molecules exist in two basic forms ($[Pt(dach)(H_2O)Cl]^+$ and $[Pt(dach)(H_2O)_2]^{2+}$) of positive charges at acidic pH values. Therefore, they display notable competitive and electrostatic repulsion with hydronium ions, which are distributed extensively on the surfaces of Mg HAP and CF/Mg HAP.[43,44]

3.2.1.2. Encapsulation duration. The effect of encapsulation time on the capacities reached by both Mg HAP and CF/Mg HAP was tested in a range from 1 h to 24 h. The other influencing factors (OXPN concentration: 200 mg L^{-1}; dosage: 20 mg; temperature: 20 °C; pH: 8; volume: 50 mL) were constant during the conducting of the tests. The OXPN encapsulation efficiencies of Mg HAP and CF/Mg HAP demonstrate remarkable enhancement in terms of both the encapsulation rates and OXPN encapsulated quantities in mg g^{-1} with regular expansion in the evaluated time interval (Fig. 4B). This enhancement impact can be observed from 1 h until 10 h; afterward, the increment in the test duration exhibits no considerable impact

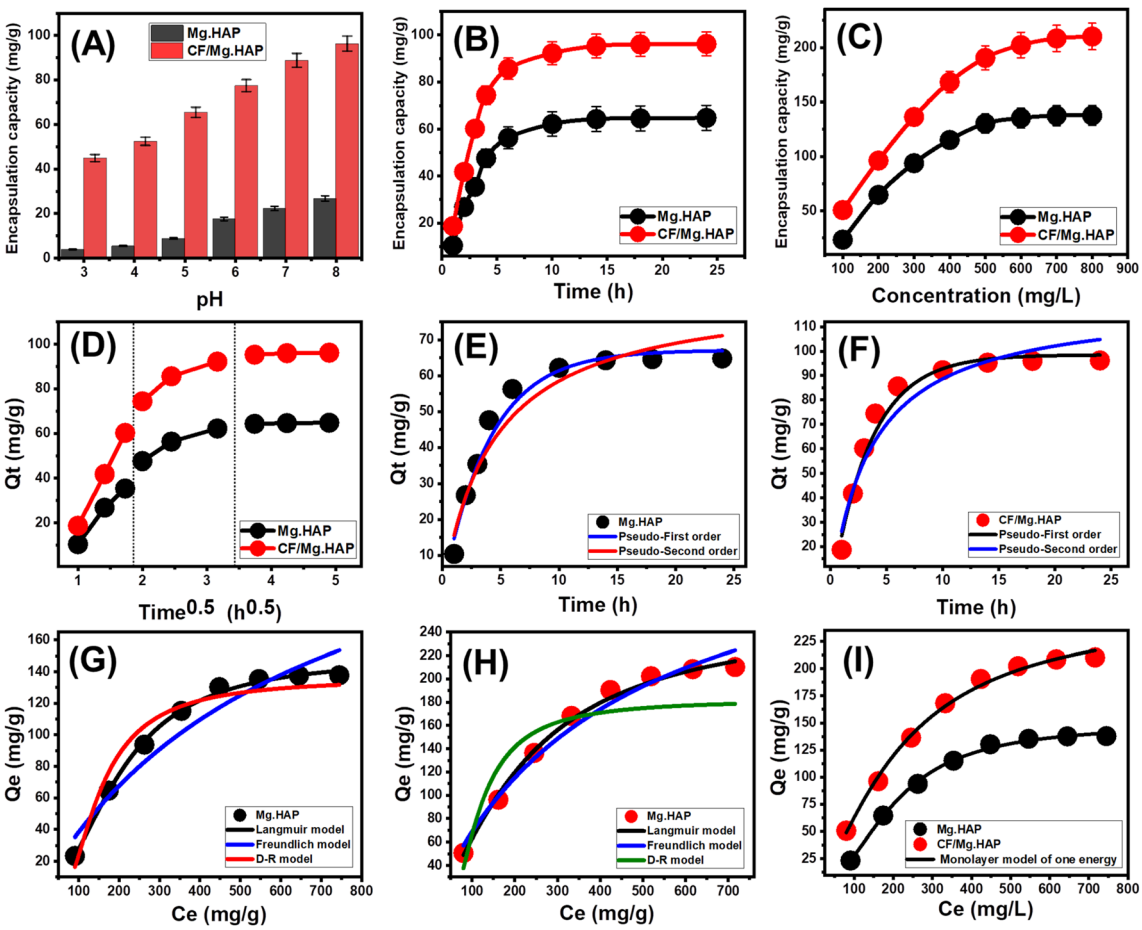

Fig. 4 Effect of the solutions pH on the encapsulation of OXPN (A), effect of encapsulation duration on the capacities of Mg HAP and CF/Mg HAP (B), effect of OXPN initial concentration on the capacities of Mg HAP and CF/Mg HAP (C), intra-particle diffusion curves of OXPN encapsulation results by Mg HAP and CF/Mg HAP (D), fitting of the OXPN encapsulation process with the kinetic models (E and F), fitting of the OXPN encapsulation process with the classic isotherm models (G and H), and fitting of the OXPN encapsulation process with advanced isotherm model (monolayer model of one energy) (I).

either on the loading rate or the OXPN encapsulated quantities, and the curves reflect stability states of nearly fixed values (Fig. 4B). Such properties signify the equilibration states of the loading systems of Mg HAP and CF/Mg HAP as potential carriers of OXPN (Mg. HAP (64.8 mg g^{-1}) and CF/Mg HAP (96.2 mg g^{-1})). The existence of active encapsulation sites in their free states and extensive quantities of Mg HAP and CF/Mg HAP at the starting intervals of the encapsulation reactions resulted in the detected high loading rates and the abrupt increase in the OXPN encapsulated quantities.[45] The progressive encapsulation of OXPN into the existing free sites of Mg HAP and CF/Mg HAP with the rising duration of the tests causes occupation and consumption of these sites, which strongly declines their availability. Therefore, the experimental encapsulation rate of OXPN dropped clearly after certain time intervals, and the incorporated Mg HAP and CF/Mg HAP particles showed an ignored enhancement in OXPN loading capacities. The loading equilibration states of Mg HAP and CF/Mg HAP were identified after the complete occupation of all the existing sites with the encapsulated OXPN molecules.[46]

3.2.1.3. OXPN concentration. The experimental impact of the assessed OXPN concentration on the achieved capacities by Mg HAP and CF/Mg HAP was followed within a tested range of 100 to 800 mg L^{-1} at adjusted values of the other affecting variables [duration: 24 h; dosage: 20 mg; temperature: 20 °C; pH: 8; volume: 50 mL]. The initial OXPN concentrations as an experimental variable during the loading processes are an essential factor in determining the maximum capacities of Mg HAP and CF/Mg HAP carriers as well as their equilibrium properties. Experimentally, the quantities of the encapsulated OXPN in Mg HAP and CF/Mg HAP increase strongly in the presence of high OXPN initial concentrations (Fig. 4C). The existence of OXPN at high concentrations within a certain volume strongly accelerates the diffusion and mobility properties of its ions, and their driving forces prompt collision chances as well as chemical interaction between the active sites of the Mg HAP and CF/Mg HAP solid particles and dissolved drug molecules.[47,48] This in turn induces the OXPN encapsulation efficiencies of Mg HAP and CF/Mg HAP until certain concentrations (500 mg L^{-1} (Mg HAP) and 700 mg L^{-1} (CF/Mg HAP) (Fig. 4C). After testing these concentrations, any increase in the evaluated OXPN concentration exhibits a neglected influence on the determined quantities of the encapsulated OXPN, which normally denote the equilibrium loading states of Mg HAP and CF/Mg HAP as potential carriers (Fig. 4C). Consequently, both Mg HAP and CF/Mg HAP reach their maximum OXPN encapsulation capacities (137.8 mg g^{-1}) (Mg HAP) and 210.8 mg g^{-1} (CF/Mg HAP). The significantly higher OXPN encapsulation capacity of Mg HAP and CF/Mg HAP was assigned to several parameters, such as (1) the reported enhancement in the surface area after the cellulose functionalization step, (2) the organophilic properties of the CF/Mg HAP as compared to hydrophilic Mg HAP, which induces its affinity to the dissolved organic molecules of OXPN, and (3) a remarkable increase in the quantities of the present and effective encapsulation sites after the integration of the cellulose chains.

3.2.2. Encapsulation mechanism

3.2.2.1. Kinetic properties

3.2.2.1.1. Intra-particle diffusion behavior. The encapsulation of OXPN into Mg HAP and CF/Mg HAP exhibits intra-particle diffusion properties of segmental shape and three visible stages without notable intersections with the original points (Fig. 4D). This demonstrates the cooperation of more than one mechanism in addition to the major impact of the ion diffusion processes on the distributed active receptors of Mg HAP and CF/Mg HAP.[48,49] These mechanisms include (A) surficial encapsulation by the active sites over the external surfaces (border), (B) the intra-particle diffusion effect, and (C) the encapsulation impact of the equilibrium state.[50] The first stage, which was reported in the curves, denotes the operation and dominant mechanistic effect of the external encapsulation, especially within the starting intervals of the reactions, and the efficiency during this stage depends mainly on the availability of the surficial active and free receptors (Fig. 4D).[51] Expanding the reaction duration results in the second segment, which signifies the operation of the OXPN diffusion processes in addition to the layered encapsulation mechanisms (Fig. 4D).[43,50] By the end of the encapsulation duration, the third stage or segment of the curves represents the equilibrium states of Mg HAP and CF/Mg HAP. This state validates the complete occupation or consumption of all the present effective binding sites with the loaded OXPN ions (Fig. 4D).[48] The encapsulation processes during this state are affected by other operating mechanisms, such as molecular interaction and/or interionic attraction processes.[47]

3.2.2.1.2. Kinetic modeling. The kinetic properties of the OXPN encapsulation process into (Mg HAP) and CF/Mg HAP were illustrated based on the kinetic assumptions of both the pseudo-first-order mode (P.F.) (eqn (4)) and the pseudo-second-order (P.S.) (eqn (5)) models. The agreement between the encapsulation processes and the kinetic models was assessed based on the non-linear fitting with their equations, considering both the correlation coefficient (R^2) and chi-squared (χ^2) as the essential indicators of the fitting degree (Table 1; Fig. 4E and F).

$$Q_t = Q_e(1 - e^{-k_1 t}) \quad (4)$$

$$Q_t = \frac{Q_e^2 k_2 t}{1 + Q_e k_2 t} \quad (5)$$

The detected values of R^2 and χ^2 indicate a higher fitting of the OXPN encapsulation processes into CF/Mg HAP with the kinetic properties of the P.F. model than the evaluated P.S. model. These fitting results were confirmed also based on the notable agreement between the previously detected experimental equilibrium capacities (Mg HAP) (64.8 mg g^{-1}) and CF/Mg HAP (96.2 mg g^{-1}) and theoretically obtained values as a mathematical parameter of the P.F. model (Mg HAP) (67.1 mg g^{-1}) and CF/Mg HAP (98.5 mg g^{-1}) (Table 1). According to the kinetic properties of the P.F. model, the encapsulation of OXPN into Mg HAP and CF/Mg HAP occurred mainly by physical

Table 1 The fitting parameters of the evaluated kinetic models, classic isotherm, advanced isotherm, van't Hof formula, and release kinetic models

Model	Parameters	Mg HAP	CF/Mg HAP
Kinetic models			
Pseudo-first-order	K_1 (min^{-1})	0.247	0.285
	$Q_{e\ (Cal)}$ (mg g^{-1})	67.1	98.5
	R^2	0.97	0.98
	X^2	0.41	0.45
Pseudo-second-order	k_2 (g mg^{-1} min^{-1})	0.0027	0.0023
	$Q_{e\ (Cal)}$ (mg g^{-1})	84.1	120.4
	R^2	0.95	0.95
	X^2	0.84	1.07
Isotherm models			
Langmuir	Q_{max} (mg g^{-1})	287.1	355.0
	b (L mg^{-1})	0.0015	0.0024
	R^2	0.94	0.98
	X^2	2.10	0.59
	R_L	0.45	0.34
Freundlich	$1/n$	0.70	0.60
	k_F (mg g^{-1})	1.52	4.58
	R^2	0.90	0.94
	X^2	3.58	1.97
D–R model	β (mol^2 kJ^{-2})	0.0446	0.0371
	Q_m (mg g^{-1})	287.4	385.4
	R^2	0.94	0.977
	X^2	2.01	0.82
	E (kJ mol^{-1})	3.35	3.67
Monolayer model of one energy	n	2.15	1.43
	Nm (mg g^{-1})	69.39	178.58
	Q_{sat} (mg g^{-1})	148.9	256.2
	ΔE (kJ mol^{-1})	−8.98	−8.74
Thermodynamics			
$\Delta G°$ (kJ mol^{-1})	293.13	−12.50	−13.68
	303.13	−12.55	−13.94
	313.13	−12.60	−14.19
	323.13	−12.64	−14.44
$\Delta H°$ (kJ mol^{-1})		−11.17	−6.27
$\Delta S°$ (J K^{-1} mol^{-1})		4.55	25.29

Release kinetics	Determination coefficient			
	Mg HAP		CF/Mg HAP	
Models	Acetate buffer (pH 5.5)	Phosphate buffer (pH 7.4)	Acetate buffer (pH 5.5)	Phosphate buffer (pH 7.4)
Zero-order	0.82	0.75	0.69	0.75
First order	0.95	0.97	0.95	0.99
Higuchi	0.95	0.97	0.90	0.92
Hixson–Crowell	0.92	0.94	0.99	0.98
Korsmeyer–Peppas	0.96	0.94	0.96	0.95
n	0.57	0.70	0.48	0.56

mechanisms that might involve strong effects of van der Waals forces and electrostatic attractions.[52,53] However, the OXPN encapsulation processes are highly fitted with the P.F. model as compared to the P.S. model, and the processes that occur still show considerable agreement with the kinetic behavior of the P.S. model. Therefore, it was expected that there would be a minor impact or assistant effect for some weak chemical processes during the OXPN encapsulation processes into Mg HAP and CF/Mg HAP, such as hydrogen bonding, hydrophobic interactions, electron sharing, and chemical complexes.[48,52] The cooperation of both physical and chemical mechanisms involved the formation of a chemically encapsulated layer of the drug, followed by the formation of a physically encapsulated layer using the first layer as substrate.[54]

3.2.2.2. Equilibrium properties

3.2.2.2.1. Classic isotherm models. The equilibrium properties of the OXPN encapsulation processes into Mg HAP and CF/Mg HAP were illustrated based on the isotherm assumptions of the Langmuir model (eqn (6)), Freundlich model (eqn (7)), and Dubinin–Radushkevich (D–R) model (eqn (8)). The agreement between the encapsulation processes and the isotherm models was assessed based on the non-linear fitting with their equations, considering both the correlation coefficient (R^2) and chi-squared (χ^2) as the essential indicators of the fitting degree (Table 1; Fig. 4G (Mg HAP) and H (CF/Mg HAP)).

$$Q_e = \frac{Q_{max}\, bC_e}{(1 + bC_e)} \quad (6)$$

$$Q_e = K_f C_e^{1/n} \quad (7)$$

$$Q_e = Q_m e^{-\beta\varepsilon^2} \quad (8)$$

The detected values of R^2 and χ^2 indicate a higher fitting of the OXPN encapsulation processes into both Mg HAP and CF/Mg HAP with the equilibrium properties of the Langmuir model than the Freundlich model. This agreement with the Langmuir isotherm suggests the homogeneous encapsulation of OXPN into the Mg HAP and CF/Mg HAP particles and in Monolayer forms.[52,53] Moreover, the estimated RL parameter of the OXPN encapsulation reaction exhibits a value less than unity, which is normally an indicator of the favorable properties of the reactions.[22,51] As an estimated parameter from the Langmuir isotherm study, the expected maximum OXPN encapsulation capacities (Q_{max}) of Mg HAP and CF/Mg HAP are 287 mg g^{-1} and 355 mg g^{-1}, respectively.

The D–R model as an equilibrium model is highly effective to elucidate the energetic heterogeneity of Mg HAP and CF/Mg HAP during the OXPN encapsulation processes regardless of the types of surfaces, either homogenous or heterogeneous.[55] The Gaussian energy (E), which was obtained as a mathematical parameter of the D–R model, considerably contributes to the nature of the OXPN encapsulation mechanisms (chemical or physical). Encapsulation processes that display an E value <8 kJ mol^{-1}, from 8 to 16 kJ mol^{-1}, and >16 kJ mol^{-1} suggest the operation of strong physical, weak chemical, complex physical/chemical, and strong chemical encapsulation mechanisms, respectively.[22,55] The values of the E parameter estimated for Mg HAP (3.35 kJ mol^{-1}) and CF/Mg HAP (3.67 kJ mol^{-1}) are within the reported range of physical mechanisms but also within the signified range of ion exchange mechanisms (0.6–25 kJ mol^{-1}), which match the theoretical findings of the kinetic studies (Table 1).

3.2.2.2.2. Advanced isotherm models. The assumptions of the advanced isotherm models according to the mathematical and physical basics of statistical physics theory strongly signify the encapsulation mechanism in terms of the surficial properties of Mg HAP and CF/Mg HAP in addition to their interactive interface with the OXPN molecules. Here, a monolayer isotherm model with one energy site (eqn (9)) was applied to describe the equilibrium properties of Mg HAP and CF/Mg HAP as potential carriers of OXPN based on their related steric and energetic parameters (Fig. 4I and Table 1).

$$Q = nN_o = \frac{nN_M}{1 + \left(\frac{C_{1/2}}{C_e}\right)^n} = \frac{Q_o}{1 + \left(\frac{C_{1/2}}{C_e}\right)^n} \quad (9)$$

The steric parameters active OXPN encapsulation sites density of Mg HAP and CF/Mg HAP ($Nm_{(OXPN)}$), number of encapsulated OXPN per one active site ($n_{(OXPN)}$), encapsulation capacities of OXPN at the saturation states of Mg HAP and CF/Mg HAP ($Q_{sat(OXPN)}$) and energetic parameter (OXPN encapsulation energy) were presented in Table 1. Based on the steric parameters, the functionalization of Mg HAP with cellulose resulted in a notable enhancement in its qualification as a potential carrier of OXPN as compared to the pure phase. The quantities of the effective free active site during the OXPN encapsulation increased strongly after the integration of cellulose ($Nm_{(OXPN)}$ = 69.4 mg g^{-1}) (Mg HAP) and 178.5 mg g^{-1} (CF/Mg HAP), which might be related to the integrated new active functional groups of cellulose or the increase in the interaction interface with the notable increase in the surface area (Table 1). The significant increase in the values of $Nm_{(OXPN)}$ of CF/Mg HAP strongly induced its loading capacity at the saturation states of its incorporated particles to be 233.6 mg g^{-1} as compared to 144.5 mg g^{-1} for Mg HAP. The detected numbers of the encapsulated OXPN ion in each free site of Mg HAP and CF/Mg HAP ($n_{(OXPN)}$ = 2.1 (Mg HAP) and 1.43 (CF/Mg HAP)) are >1, suggesting the vertical orientation of the loaded ions and their encapsulation by multimolecular mechanisms (Table 1).[56,57]

The energies of the OXPN encapsulation processes (ΔE) into Mg HAP and CF/Mg HAP were determined based on eqn (10) considering OXPN rest concentration at the half saturations of Mg HAP and CF/Mg HAP ($C_{1/2}$) as well as the absolute solubility of OXPN (Table 1).

$$\Delta E = -RT \ln\left(\frac{S}{C_{1/2}}\right) \quad (10)$$

The estimated values of ΔE during the OXPN processes using Mg HAP and CF/Mg HAP are −8.98 kJ mol^{-1} and −8.74 kJ mol^{-1}, respectively. These energetic values significantly match the previously reported suggestion based on the kinetic and classic isotherm studies about the essential mechanistic impact of the physical processes and weak chemical reactions, as the ΔE values are ≤40 kJ mol^{-1}.[56] The effective mechanistic processes might involve van der Waals forces (ΔE = 4 to 10 kJ mol^{-1}), dipole bonding forces (ΔE = 2 to 29 kJ mol^{-1}), and hydrogen bonding (ΔE < 30 kJ mol^{-1}).[58,59] This might involve electrostatic attractions and hydrogen bonding between the OXPN amino groups and hydroxyl groups of hydroxyapatite and cellulose fibers.

3.2.2.3. Thermodynamic properties. The thermodynamic properties of the OXPN encapsulation reactions by Mg HAP and CF/Mg HAP were evaluated considering the temperature range from 20 °C to 50 °C at adjusted values of the other affecting

variables [duration: 24 h; dosage: 20 mg; concentration: 800 mg L^{-1}; pH: 8; volume: 50 mL]. The thermodynamic properties involved essential functions such as Gibbs free energy ($\Delta G°$) (eqn (12)) in addition to the entropy ($\Delta S°$) and enthalpy ($\Delta H°$) of the reactions, which were determined as parameters from the linear regression fitting with the vant Hof equation (eqn (12)) (Fig. 5).[60]

$$\ln(K_c) = \frac{\Delta S^\circ}{R} - \frac{\Delta H^\circ}{RT} \quad (11)$$

$$\Delta G^\circ = -RT \ln K_c \quad (12)$$

The detection of $\Delta G°$ and $\Delta H°$ with negatively signed values reveals the spontaneous, exothermic, and favorable behaviors of the OXPN encapsulation reactions either by Mg HAP or CF/Mg HAP (Table 1). Moreover, the positively signed $\Delta S°$ values using both Mg HAP and CF/Mg HAP declared the increment in the randomness of the OXPN encapsulation reactions in terms of the tested temperature.

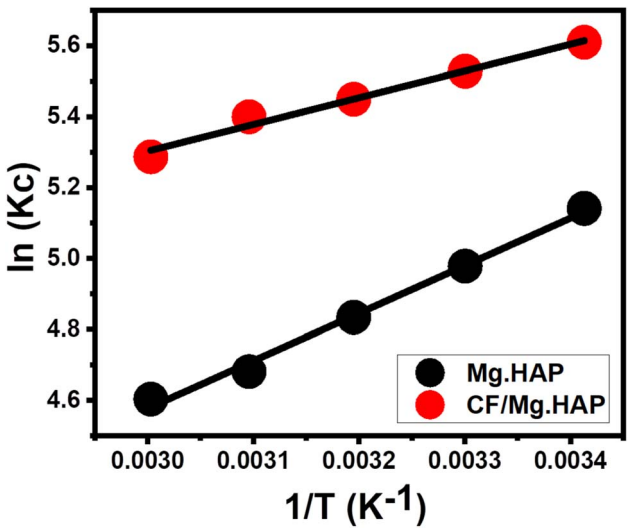

Fig. 5 Fitting of the OXPN encapsulation results with van't Hof thermodynamic equation.

3.3. *In vitro* release profiles

The OXPN release properties from the structures of Mg HAP and CF/Mg HAP were assessed based on the determined percentage of the drug released within the two buffers used (phosphate (pH 7.4) and acetate (pH 5.5)) to simulate the environment and conditions of the tumor cells (Fig. 6). The measured determined percentage of the drug released from both Mg HAP and CF/Mg HAP with the two studied buffers validates observable changes in the recognized rates with a significant increment in the assessed release duration (Fig. 6A and B). The OXPN release rates from Mg HAP and CF/Mg HAP exhibit fast properties, which are associated with remarkable changes in the released quantities of OXPN. After certain release intervals, the actual OXPN diffusion rates weakened notably, and no considerable increase in released qualities could be detected. This finally appeared to be fixed by the end of the tests. The rapid OXPN diffusion rates during the beginning release intervals were assigned to the fast desorption of the molecules of the drug immediately from the weakly bonded and physically encapsulated OXPN ions by the surficial adsorption sites of Mg HAP and CF/Mg HAP.[61–63] After the complete desorption of the weakly bonded and surficially loaded OXPN molecules, the release properties became controlled by the diffusion of the strongly bonded molecules in chemically complexed forms, in addition to the trapped OXPN ions within the structural pores of hydroxyapatite, which adversely affected the determined diffusion rates.[5,60,64] Furthermore, the observed OXPN release profiles of Mg HAP and CF/Mg HAP reflected a significant accelerating impact of the acidic conditions (pH 5.5 (acetate buffer)) on the release process as compared to the basic conditions (pH 7.4 (phosphate buffer)). The faster OXPN release properties at pH 5.5 than at pH 7.4 were attributed to the notable enhancement in the drug's mobility, solubility, and diffusion properties with the decline in pH.[16] Additionally, the expected degradation effect of the low pH condition on the structure of HAP induces its fast-release properties.[65]

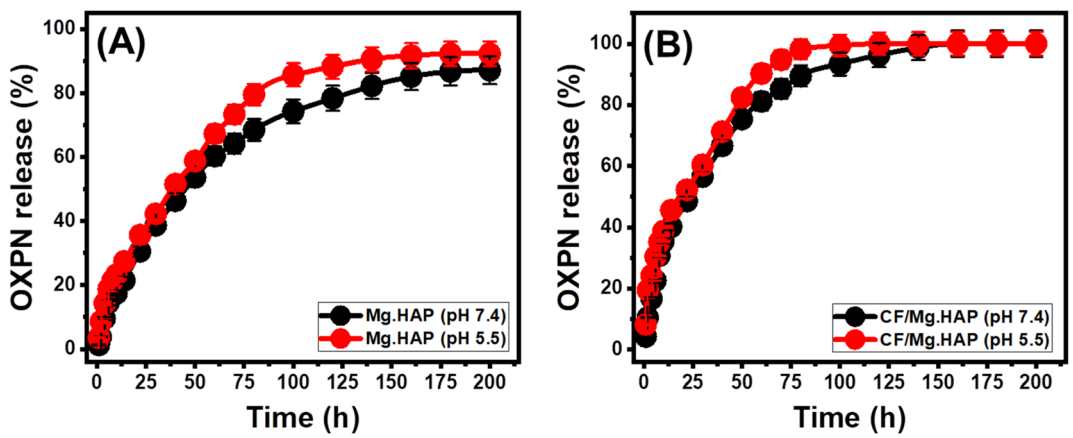

Fig. 6 The OXPN release profiles of Mg HAP and CF/Mg HAP at the acetate buffer (pH 5.5) (A) and phosphate buffer (pH 7.4) (B).

The experimental OXPN release profiles of Mg HAP either in the phosphate buffer or the acetate buffer extended to about 200 h without any experimental detection of the complete release states (100% release percentage) (Fig. 6A and B). About 50% of the encapsulated quantity of OXPN was diffused from the structure of Mg HAP after 40 h and 50 h at pH 5.5 and pH 7.4, respectively. The maximum OXPN release percentages in the phosphate buffer and the acetate buffer after 200 h are 92.3% and 87.2%, respectively. Regarding the profiles of CF/Mg HAP and Mg HAP, CF/Mg HAP shows notably faster release properties than Mg HAP (Fig. 6A and B). About 50% of the encapsulated quantity of OXPN was diffused from the structure of CF/Mg HAP after 22 h and 30 h at pH 5.5 and pH 7.4, respectively. However, the complete diffusion in the acetate buffer was detected after about 120 h, and the complete diffusion in the phosphate buffer was detected after 160 h.

The higher release rate property of OXPN from Mg HAP and CF/Mg HAP signifies strongly the remarkable impact of the integrated cellulose structure on the properties of hydroxyapatite (Fig. 6A and B). The common formation of chemical complexes and hydrogen bonds between the active functional groups of OXPN and the reactive hydroxyl groups of hydroxyapatite, in addition to the expected trapping of the drug ions within its structural nanopores, exhibits a strong adverse effect on the efficiency of the diffusion or desorption reactions of the encapsulated ions.[4,65] Therefore, the functionalization process of Mg HAP with cellulose provides considerable barriers between the drug and the reactive groups of hydroxyapatite, which reduce the quantities of the formed complexes as well as the quantities of the trapped ions.[4,63,65] Moreover, the integrated cellulose fibers provided additional free sites for surficial loading processes, which also prompt the release properties. The slow and controlled delivery of OXPN as anticancer chemotherapy drug was recommended in specific cases that required long-term interaction and exposure between the drug ions and the tumor cells.[5,6] Also, very fast and abrupt delivery processes are recommended in some cases that require certain therapeutic dosages within short intervals. Therefore, the synthetic CF/Mg HAP as a potential carrier of OXPN can provide a favorable delivery system that exhibits controlled encapsulation and release properties.

3.4. Release kinetic studies

The kinetic studies of the OXPN release processes from Mg HAP and CF/Mg HAP were performed as indications about the controlled mechanistic processes. Modeling of the release processes according to zero-order (Z–O) (eqn (13)), first-order (F–O) (eqn (14)), Higuchi (H–G) (eqn (15)), Hixson–Crowell (H–C) (eqn (16)), and Korsmeyer–Peppas (K–P) (eqn (17)) release kinetic models was used to illustrate the mechanisms based on the linear regression fitting degrees with these models.[5]

$$W_t - W_0 = K_0 t \quad (13)$$

$$\ln(W_\infty / W_t) = K_1 t \quad (14)$$

$$W_t = K_h t^{1/2} \quad (15)$$

$$W_o^{1/3} - W_t^{1/3} = K_{HC} t \quad (16)$$

$$W_t / W_\infty = K_p t^n \quad (17)$$

The zero-order kinetic properties validate the occurrence of the release at constant rates without the considerable impact of the dosages of the loaded OXPN drug on the release efficiencies of Mg HAP and CF/Mg HAP.[4] Regarding the F–O release kinetics, the OXPN-encapsulated dosages into Mg HAP and CF/Mg HAP strongly affect the release efficiencies.[1] The mechanistic assumption of Higuchi kinetics (H–G) determines the dominant impact of the diffusion mechanisms during the release processes.[1,66] The diffusion mechanisms, according to the Higuchi kinetics, occurred at a fixed rate, which is lower than the encapsulated OXPN quantities. Moreover, the used carriers must exhibit sink properties, and their swelling and solubility display a neglected impact on the release behaviors.[4] The mechanistic assumption of the Hixson–Crowell model (H–C) involves erosion rather than diffusion, with significant influence on the surface area and diameter of the tested particles of the carriers.[4,67] Regarding the mechanistic assumption of Korsmeyer–Peppas kinetics, the release processes involve the cooperation of diffusion and erosion mechanisms.[1,68]

Based on the determination coefficients (R^2), the OXPN release mechanisms of Mg HAP and CF/Mg HAP follow the properties of the F–O (Fig. 7C and D; Table 1) model rather than the Z–O model (Fig. 7A and B; Table 1) reflecting the strong influence of the encapsulated OXPN dosages on the release performances. The release behaviors show excellent agreement with both Higuchi (H–G) (Fig. 7E and F; Table 1) and Hixson–Crowell (H–C) models (Fig. 7G and H; Table 1). These kinetic assessment results suggested the cooperation of diffusion and erosion processes during the OXPN release. However, while the release profile of Mg HAP exhibits a slightly higher agreement with Higuchi kinetics, reflected by the dominant effect of diffusion mechanisms, the profile of CF/Mg HAP slightly follows Hixson–Crowell kinetics and is affected essentially by erosion mechanisms. This mechanistic suggestion was supported by the recognized significant fitting degrees of the Korsmeyer–Peppas and the estimated values of the diffusion exponent (n) as a fitting parameter (Fig. 7I; Table 1). The values of the diffusion exponent (n) are higher than 0.45, validating non-Fickian transport properties of the release processes of Mg HAP and CF/Mg HAP delivery systems.[45]

3.5. Cytotoxicity properties

The cytotoxic effect of the free Mg HAP and CF/Mg HAP particles on normal colorectal fibroblast cells (CCD-18Co) was evaluated as an essential factor to assess the biocompatibility and safety value of the studied cancer on normal and non-infected cells. The cytotoxicity of free CF/Mg HAP particles, as well as their OXPN-loaded products, was evaluated against the target human colorectal cancer cell (HCT-116) to determine its value as an anticancer agent and as a carrier of enhanced impact on the therapeutic effect of the loaded OXPN drug. Regarding the cytotoxic effect of free CF/Mg HAP particles on the CCD-18Co

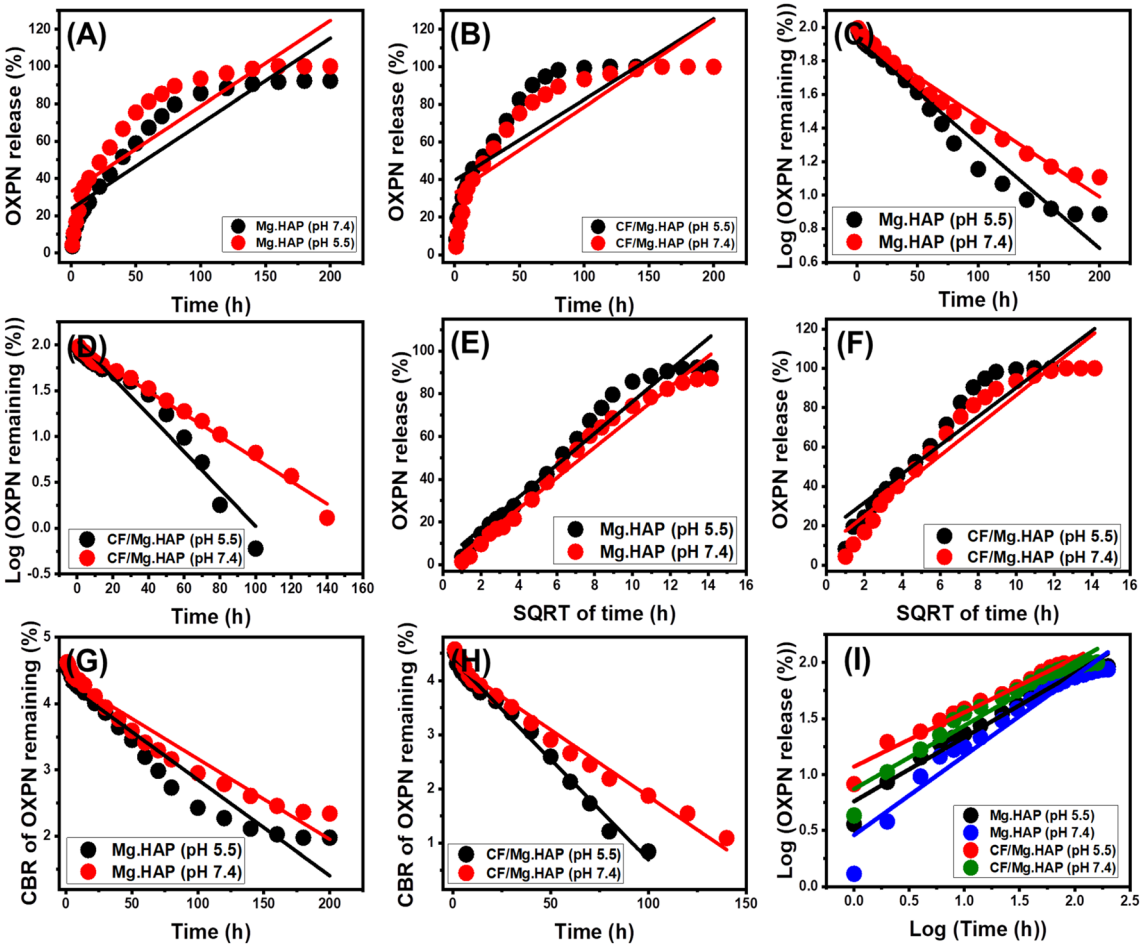

Fig. 7 Fitting of the OXPN release results with zero-order model (A and B), first-order model (C and D), higuchi model (E and F), Hixson–Crowell model (G and H), and Korsmeyer–Peppas model (I).

normal cells, the composite particles display high biocompatible and safe properties on the normal cell lines within the evaluated experimental range of the applied dosages (20 to 120 μg L^{-1}). The measured cell viability percentages during the treatment of the CCD-18Co normal cells with the highest tested dosage of the free Mg HAP and CF/Mg HAP particles (120 μg L^{-1}) are 92.3% and 87.6%, respectively.

Regarding the cytotoxic impacts of the free Mg HAP and CF/Mg HAP particles on the infected HCT-116 cells, the synthetic composite as free particles displays considerable cytotoxicity against the tumor cells, especially at the applied dosages higher than 50 μg mL^{-1} (Fig. 8). The measured cell viability percentage, inhibitory percentage, and IC-50 value in the presence of 500 μg mL^{-1} of free Mg HAP particles are 33.62%, 66.38%, and 157.18 μg mL^{-1} respectively (Fig. 8A), while the reported values of free CF/Mg HAP are 21.82% (cell viability), 78.18% (inhibitory percentage), and 121.15 μg mL^{-1} (IC-50 value) (Fig. 8B). Such cytotoxic results validate the promising biological activity of Mg HAP, which is enhanced at a considerable rate after its functionalization with cellulose (CF/Mg HAP). Regarding the cytotoxicity properties of OXPN-encapsulated CF/Mg HAP against HCT-116 cancer cells, the application of the same dosage of the free particles (500 μg mL^{-1}) resulted in 1.85% cell viability percentage, 98.15% inhibitory percentage, and 30.7 μg mL^{-1} as IC-50 (Fig. 8C). Such cytotoxic results demonstrate the remarkable enhancement impact of the used CF/Mg HAP carrier on the cytotoxic effects and the therapeutic impact of the loaded OXPN drug as common chemotherapy drug, in addition to its previously determined controlling effects on the loading and release behaviors.[69]

3.6. Comparative study

The comparative analysis of loading capacities and release profiles of CF/Mg HAP as a potential carrier for OXPN was conducted in relation to other carriers explored in previous studies (Table 2). In terms of loading capacity, the synthetic CF/Mg HAP composite exhibits superior loading capabilities for OXPN in comparison to pure HAP and magnesium modified HAP, as well as most of the presented structures (Table 2). The release patterns of the CF/Mg HAP composite exhibit notable faster properties in comparison to the release profiles of HAP and Mg HAP and considerable rate considering the properties of the other investigated structure.

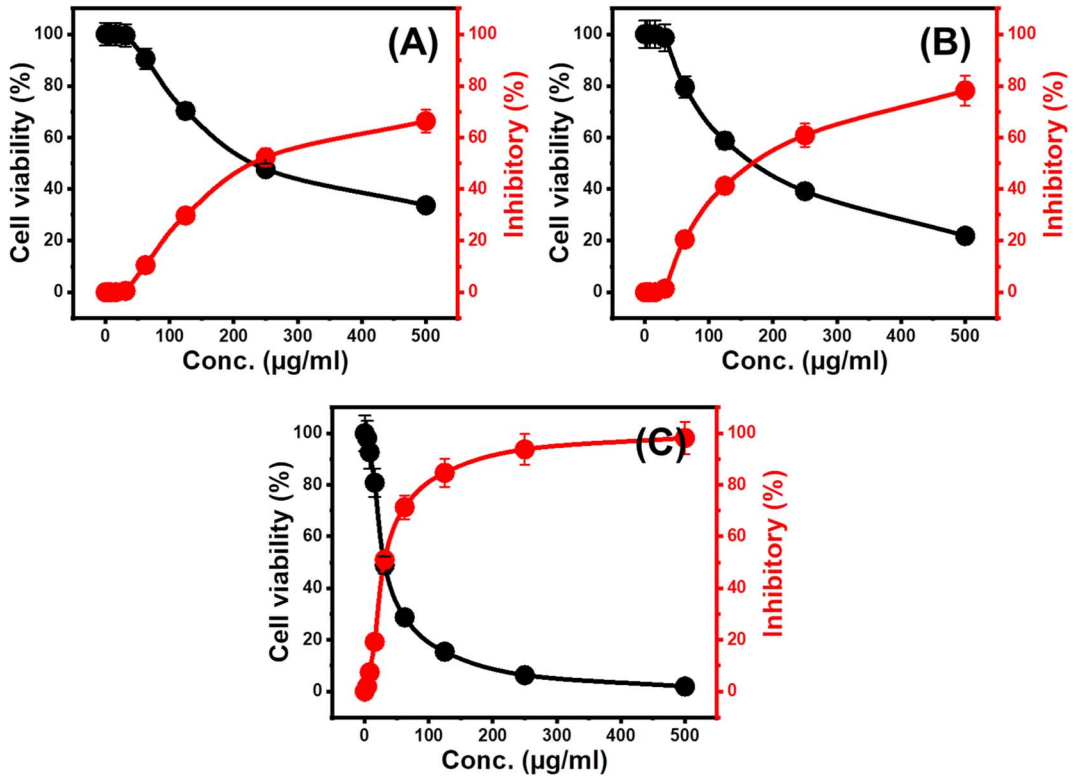

Fig. 8 The cytotoxicity effect of free Mg HAP (A), free CF/Mg HAP composite (B), and OXPN encapsulated CF/Mg HAP (C) on colorectal cancer cell (HCT-116).

Table 2 Comparison between the loading and release properties of CS/Di composite and other investigated carriers in literature

Carrier	Loading capacity (mg g^{-1})	Release period (h)	References
Hydroxyapatite	49.1	—	70
Cellulose/zeolite-A	285.7	150 h	71
Zeolite-A	109.03	150 h	71
Phillipsite	79.6	180 h	11
Diatomite	65.9	200 h	72
HAP	**53.3**	**200 h**	**This study**
Mg HAP	**69.4**	**200 h**	**This study**
CF/Mg HAP	**178.58**	**160 h**	**This study**

4. Conclusion

Synthetic magnesium-doped hydroxyapatite (Mg HAP) was hybridized with cellulose, forming an innovative structure (CF/Mg HAP), which was characterized as a potential multifunctional carrier of oxaliplatin (OXPN) chemotherapy drug. CF/Mg HAP exhibit enhanced OXPN encapsulation properties (256.2 mg g^{-1}) than Mg HAP (148.9 mg g^{-1}). This was assigned to the enhancement in organic affinity, surface area, and active site density (178.58 mg g^{-1} (CF/Mg HAP) and 69.39 mg g^{-1} (Mg HAP)). The loading process into CF/Mg HAP involved the encapsulation of two OXPN molecules per site. The encapsulation process is controlled by physical mechanisms, such as according to the energy of the reaction (<40 kJ mol^{-1}). The release profile of CF/Mg HAP shows slow and controlled properties for more than 100 h. This occurred according to complex erosion/diffusion mechanisms based on the release kinetics and diffusion exponent (>0.45). The cell viability of HCT-116 cancer cells after treatment with free CF/Mg HAP (21.82%) and OXPN-loaded products (1.85%) reflected strong inhibition effects on the cancer cells.

5. Recommendation

Further studies will be conducted to evaluate the biological and anticancer activities of hydroxyapatite doped with other types of metals, as well as their properties as drug delivery systems for chemotherapy drugs, considering their cytotoxic effect on normal cells.

Conflicts of interest

The authors declare that there is no conflict in interest.

Acknowledgements

The authors acknowledge the Deanship of Scientific Research at Imam Mohammad Ibn Saud Islamic University (IMSIU) (grant number IMSIU-RP23021). Also the authors acknowledge Princess Nourah Bint Abdulrahman University Researchers Supporting Project number (PNURSP2023R400), Princess Nourah bint Abdulrahman University, Riyadh, Saudi Arabia.

References

1 H. M. El-Zeiny, M. R. Abukhadra, O. M. Sayed, A. H. Osman and S. A. Ahmed, Insight into novel β-cyclodextrin-grafted poly (Nvinylcaprolactam) nanogel structures as advanced carriers for 5- fluorouracil: Equilibrium behavior and pharmacokinetic modeling, *Colloids Surf., A*, 2020, **586**, 124197.

2 Y. Demir, C. Türkeş and S. Beydemir, Molecular docking studies and inhibition properties of some antineoplastic agents against paraoxonase-I, *Anti-Cancer Agents Med. Chem.*, 2020, **20**(7), 887–896.

3 T. Sun, W. Cui, M. Yan, G. Qin, W. Guo, H. Gu, S. Liu and Q. Wu, Target Delivery of a Novel Antitumor Organoplatinum (IV)-Substituted Polyoxometalate Complex for Safer and More Effective Colorectal Cancer Therapy In Vivo, *Adv. Mater.*, 2016, **28**(34), 7397–7404.

4 S. I. Othman, A. A. Allam, H. AlFassam, G. M. Abu-Taweel, N. Altoom and M. R. Abukhadra, Sonoco green decoration of clinoptilolite with MgO nanoparticles as a potential carrier for 5-fluorouracil drug: loading behavior, release profile, and cytotoxicity, *J. Inorg. Organomet. Polym.*, 2021, **31**, 4608–4622.

5 L. Tian, M. R. Abukhadra, A. S. Mohamed, A. Nadeem, S. F. Ahmad and K. E. Ibrahim, Insight into the loading and release properties of an exfoliated kaolinite/cellulose fiber (EXK/CF) composite as a carrier for oxaliplatin drug: cytotoxicity and release kinetics, *ACS Omega*, 2020, **5**(30), 19165–19173.

6 P. Sundaramoorthy, T. Ramasamy, S. K. Mishra, K. Y. Jeong, C. S. Yong, J. O. Kim and H. M. Kim, Engineering of caveolae-specific self-micellizing anticancer lipid nanoparticles to enhance the chemotherapeutic efficacy of oxaliplatin in colorectal cancer cells, *Acta Biomater.*, 2016, **42**, 220–231.

7 R. A. Praphakar, M. Jeyaraj, S. Mehnath, A. Higuchi, D. Ponnamma, K. K. Sadasivuni and M. Rajan, A pH-sensitive guar gum-grafted-lysine-β-cyclodextrin drug carrier for the controlled release of 5-fluorouracil into cancer cells, *J. Mater. Chem.*, 2018, **6**, 1519–1530.

8 J. E. Lee, S. M. Abuzar, Y. Seo, H. Han, Y. Jeon, E. J. Park, S. H. Baik and S. J. Hwang, Oxaliplatin-loaded chemically cross-linked hydrogels for prevention of postoperative abdominal adhesion and colorectal cancer therapy, *Int. J. Pharm.*, 2019, **565**, 50–58.

9 A. M. Itoo, M. Paul, B. Ghosh and S. Biswas, Oxaliplatin delivery via chitosan/vitamin E conjugate micelles for improved efficacy and MDR-reversal in breast cancer, *Carbohydr. Polym.*, 2022, **282**, 119108.

10 Y. Li, Z. Sun, Y. Cui, H. Zhang, S. Zhang, X. Wang, S. Liu and Q. Gao, Oxaliplatin derived monofunctional triazole-containing platinum (II) complex counteracts oxaliplatin-induced drug resistance in colorectal cancer, *Bioorg. Chem.*, 2021, **107**, 104636.

11 N. Altoom, S. M. Ibrahim, S. I. Othman, A. A. Allam, H. A. Alqhtani, F. S. Al-Otaibi and M. R. Abukhadra, Characterization of β-cyclodextrin/phillipsite (β-CD/Ph) composite as a potential carrier for oxaliplatin as therapy for colorectal cancer; loading, release, and cytotoxicity, *Colloids Surf., A*, 2022, **648**, 129144.

12 P. Taslimi, F. M. Kandemir, Y. Demir, M. İleritürk, Y. Temel, C. Caglayan and I. Gulçin, The antidiabetic and anticholinergic effects of chrysin on cyclophosphamide-induced multiple organ toxicity in rats: Pharmacological evaluation of some metabolic enzyme activities, *J. Biochem. Mol. Toxicol.*, 2009, **33**(6), e22313.

13 H. Ceylan, Y. Demir and S. Beydemir, Inhibitory effects of usnic and carnosic acid on some metabolic enzymes: an in vitro study, *Protein Pept. Lett.*, 2019, **26**(5), 364–370.

14 Y. Ren, X. Li, B. Han, N. Zhao, M. Mu, C. Wang, Y. Du, Y. Wang, A. Tong, Y. Liu and L. Zhou, Improved anti-colorectal carcinomatosis effect of tannic acid co-loaded with oxaliplatin in nanoparticles encapsulated in thermosensitive hydrogel, *Eur. J. Pharm. Sci.*, 2019, **128**, 279–289.

15 N. Alamer, A. Meshkini, L. Khoshtabiat and A. Behnamsani, Synergizing effects of chemodynamic therapy and chemotherapy against breast cancer by oxaliplatin-loaded polydopamine/BSA@ copper ferrite, *J. Drug Delivery Sci. Technol.*, 2022, **72**, 103391.

16 A. Narmani, M. Kamali, B. Amini, A. Salimi and Y. Panahi, Targeting delivery of oxaliplatin with smart PEG-modified PAMAM G4 to colorectal cell line: In vitro studies, *Process Biochem.*, 2018, **69**, 178–187.

17 S. P. Bandi and V. V. K. Venuganti, Functionalized polymeric patch for localized oxaliplatin delivery to treat gastric cancer, *Mater. Sci. Eng., C*, 2021, **128**, 112302.

18 A. Kumar, Y. S. Negi, V. Choudhary and N. K. Bhardwaj, Microstructural and mechanical properties of porous biocomposite scaffolds based on polyvinyl alcohol, nano-hydroxyapatite and cellulose nanocrystals, *Cellulose*, 2014, **21**, 3409–3426.

19 S. C. Veerla, J. Kim, H. Sohn and S. Y. Yang, Controlled nanoparticle synthesis of Ag/Fe co-doped hydroxyapatite system for cancer cell treatment, *Mater. Sci. Eng., C*, 2019, **98**, 311–323.

20 M. Lelli, N. Roveri, C. Marzano, J. D. Hoeschele, A. Curci, N. Margiotta, V. Gandin and G. Natile, Hydroxyapatite nanocrystals as a smart, pH sensitive, delivery system for kiteplatin, *Dalton Trans.*, 2016, **45**(33), 13187–13195.

21 S. M. Huang, S. M. Liu, C. L. Ko and W. C. Chen, Advances of Hydroxyapatite Hybrid Organic Composite Used as Drug or Protein Carriers for Biomedical Applications: A Review, *Polymers*, 2022, **14**(5), 976.

22 I. R. Sayed, A. M. Farhan, A. A. AlHammadi, M. I. El-Sayed, I. M. Abd El-Gaied, A. M. El-Sherbeeny, W. Al Zoubi, Y. G. Ko and M. R. Abukhadra, Synthesis of novel nanoporous zinc phosphate/hydroxyapatite nano-rods (ZPh/HPA_{NRs}) core/shell for enhanced adsorption of Ni^{2+} and Co^{2+} ions: Characterization and application, *J. Mol. Liq.*, 2022, **360**, 119527.

23 E. A. Ofudje, A. E. Adedapo, O. B. Oladeji, E. F. Sodiya, F. H. Ibadin and D. Zhang, Nano-rod hydroxyapatite for the uptake of nickel ions: Effect of sintering behaviour on

adsorption parameters, *J. Environ. Chem. Eng.*, 2021, **9**(5), 105931.

24 S. Pai, M. S. Kini, R. Mythili and R. Selvaraj, Adsorptive removal of AB113 dye using green synthesized hydroxyapatite/magnetite nanocomposite, *Environ. Res.*, 2022, **210**, 112951.

25 S. Pujari-Palmer, S. Chen, S. Rubino, H. Weng, W. Xia, H. Engqvist, L. Tang and M. K. Ott, In vivo and in vitro evaluation of hydroxyapatite nanoparticle morphology on the acute inflammatory response, *Biomaterials*, 2016, **90**, 1–11.

26 T. N. Tran, Q. C. Do, D. Kim, J. Kim and S. Kang, Urchin-like structured magnetic hydroxyapatite for the selective separation of cerium ions from aqueous solutions, *J. Hazard. Mater.*, 2022, **430**, 128488.

27 Y. Wan, T. Cui, G. Xiong, W. Li, J. Tu, Y. Zhu and H. Luo, Magnetic lamellar nanohydroxyapatite as a novel nanocarrier for controlled delivery of 5-fluorouracil, *Ceram. Int.*, 2017, **43**(6), 4957–4964.

28 L. Fan, W. Kong, C. Gao and P. Zhu, Synthesis of highly porous iron-doped carbonated hydroxyapatite spheres for efficient adsorption of carmine dyes, *Materialia*, 2021, **20**, 101205.

29 E. Mossavi, M. H. Sabzevari, M. Ghaedi and M. A. Azqhandi, Adsorption of the azo dyes from wastewater media by a renewable nanocomposite based on the graphene sheets and hydroxyapatite/ZnO nanoparticles, *J. Mol. Liq.*, 2022, **350**, 118568.

30 E. W. Elsayed, A. A. El-Ashmawy, G. T. El-Bassyouni, S. M. Mousa, M. El-Manawaty and L. H. Emara, Formulation and evaluation of alginate-gelatin hydrogel scaffolds loaded with zinc-doped hydroxyapatite and 5-fluorouracil, *Int. J. Biol. Macromol.*, 2023, 124147.

31 M. Pooresmaeil, S. Javanbakht, S. B. Nia and H. Namazi, Carboxymethyl cellulose/mesoporous magnetic graphene oxide as a safe and sustained ibuprofen delivery bio-system: Synthesis, characterization, and study of drug release kinetic, *Colloids Surf., A*, 2020, **594**, 124662.

32 L. Bandura, M. Białoszewska, S. Malinowski and W. Franus, Adsorptive performance of fly ash-derived zeolite modified by β-cyclodextrin for ibuprofen, bisphenol A and caffeine removal from aqueous solutions–equilibrium and kinetic study, *Appl. Surf. Sci.*, 2021, **562**, 150160.

33 M. Rahaman, M. Rahman, S. M. Alam, M. Sultana, M. Parvez and A. Ahmed, Preparation and Characterization of Mustard Stalks Derived Carboxymethyl Cellulose and Poly (L-Lactic Acid) Biocomposites. Masud and Ahmed, Asadullah, Preparation and Characterization of Mustard Stalks Derived Carboxymethyl Cellulose and Poly (L-Lactic Acid) Biocomposites, *Organic Chemistry eJournal*, 2021, DOI: 10.2139/ssrn.3899839.

34 A. T. Okasha, A. A. Abdel-Khalek, A. M. El-Sherbeeny, W. Al Zoubi and M. R. Abukhadra, Advanced equilibrium study on the synthesis and characterization of Mg-doped hydroxyapatite nano-fibers as a potential enhanced adsorbent of Zn (II) and malachite green dye, *Mater. Today Commun.*, 2023, 105883.

35 Y. Zhou, W. Li, X. Jiang, Y. Sun, H. Yang, Q. Liu, Y. Cao, Y. Zhang and H. Cheng, Synthesis of strontium (Sr) doped hydroxyapatite (HAp) nanorods for enhanced adsorption of Cr (VI) ions from wastewater, *Ceram. Int.*, 2021, **47**(12), 16730–16736.

36 T. Xiong, Q. Li, J. Liao, Y. Zhang and W. Zhu, Highly enhanced adsorption performance to uranium (VI) by facile synthesized hydroxyapatite aerogel, *J. Hazard. Mater.*, 2022, **423**, 127184.

37 R. Foroutan, S. J. Peighambardoust, A. Ahmadi, A. Akbari, S. Farjadfard and B. Ramavandi, Adsorption mercury, cobalt, and nickel with a reclaimable and magnetic composite of hydroxyapatite/Fe3O4/polydopamine, *J. Environ. Chem. Eng.*, 2021, **9**(4), 105709.

38 D. Mehta, P. Mondal, V. K. Saharan and S. George, In-vitro synthesis of marble apatite as a novel adsorbent for removal of fluoride ions from ground water: an ultrasonic approach, *Ultrason. Sonochem.*, 2018, **40**, 664–674.

39 P. T. Nguyen, X. T. Nguyen, T. V. Nguyen, T. T. Nguyen, T. Q. Vu, H. T. Nguyen, N. T. Pham and T. M. Thi Dinh, Treatment of Cd^{2+} and Cu^{2+} ions using modified apatite ore, *J. Chem.*, 2020, **2020**, 6527197.

40 Y. Chen, M. Li, Y. Li, Y. Liu, Y. Chen, H. Li, L. Li, F. Xu, H. Jiang and L. Chen, Hydroxyapatite modified sludge-based biochar for the adsorption of Cu^{2+} and Cd^{2+}: adsorption behavior and mechanisms, *Bioresour. Technol.*, 2021, **321**, 124413.

41 K. Ullah, S. A. Khan, G. Murtaza, M. Sohail, A. Manan and A. Afzal, Gelatin-based hydrogels as potential biomaterials for colonic delivery of oxaliplatin, *Int. J. Pharm.*, 2019, **556**, 236–245.

42 C. Liang, H. Wang, M. Zhang, W. Cheng, Z. Li, J. Nie, G. Liu, D. Lian, Z. Xie, L. Huang and X. Zeng, Self-controlled release of oxaliplatin prodrug from d- α-tocopheryl polyethylene glycol 1000 succinate (TPGS) functionalized mesoporous silica nanoparticles for cancer therapy, *J. Colloid Interface Sci.*, 2018, **525**, 1–10.

43 M. R. Abukhadra, F. A. El Kashief, S. I. Othman, H. A. Alqhtani and A. A. Allam, Synthesis and characterization of Fe^0@ chitosan/cellulose biocompatible composites from natural resources as advanced carriers for ibuprofen drug: reaction kinetics and equilibrium, *New J. Chem.*, 2022, **46**(26), 12797–12807.

44 K. Lenz, S. Hann, G. Koellensperger, Z. Stefanka, G. Stingeder, N. Weissenbacher, S. N. Mahnik and M. Fuerhacker, Presence of cancerostatic platinum compounds in hospital wastewater and possible elimination by adsorption to activated sludge, *Sci. Total Environ.*, 2005, **345**(1–3), 141–152.

45 M. R. Abukhadra, N. M. Refay, A. M. El-Sherbeeny, A. M. Mostafa and M. A. Elmeligy, Facile synthesis of bentonite/biopolymer composites as low-cost carriers for 5-fluorouracil drug; equilibrium studies and pharmacokinetic behavior, *Int. J. Biol. Macromol.*, 2019, **141**, 721–731.

46 M. Salam, M. Mokhtar, S. M. Albukhari, D. F. Baamer, L. Palmisano, M. Jaremko and M. R. Abukhadra, Synthesis

and Characterization of Green ZnO@ polynaniline/ Bentonite Tripartite Structure (G. Zn@ PN/BE) as Adsorbent for As (V) Ions: Integration, Steric, and Energetic Properties, *Polymers*, 2022, **14**(12), 2329.

47 Y. Jiang, M. R. Abukhadra, N. M. Refay, M. F. Sharaf, M. A. El-Meligy and E. M. Awwad, Synthesis of chitosan/MCM-48 and β-cyclodextrin/MCM-48 composites as bio-adsorbents for environmental removal of Cd^{2+} ions; kinetic and equilibrium studies, *React. Funct. Polym.*, 2020, **154**, 104675.

48 M. A. Salam, M. R. Abukhadra and M. Mostafa, Effective decontamination of As (V), Hg (II), and U (VI) toxic ions from water using novel muscovite/zeolite aluminosilicate composite: adsorption behavior and mechanism, *Environ. Sci. Pollut. Res.*, 2020, **27**(12), 13247–13260.

49 E. El Qada, Kinetic Behavior of the Adsorption of Malachite Green Using Jordanian Diatomite as Adsorbent, *Jordanian J. Eng. Chem. Ind.*, 2020, **3**(1), 1–10.

50 X. Lin, Y. Xie, H. Lu, Y. Xin, R. Altaf, S. Zhu and D. Liu, Facile preparation of dual La-Zr modified magnetite adsorbents for efficient and selective phosphorus recovery, *Chem. Eng. J.*, 2021, **413**, 127530.

51 S. M. Albukhari, M. A. Salam and M. R. Abukhadra, Effective retention of inorganic Selenium ions (Se (VI) and Se (IV)) using novel sodalite structures from muscovite; characterization and mechanism, *J. Taiwan Inst. Chem. Eng.*, 2021, **120**, 116–126.

52 A. Sherlala, M. M. Raman and A. Bello, Buthiyappan, Adsorption of arsenic using chitosan magnetic graphene oxide nanocomposite, *J. Environ. Manage.*, 2019, **246**, 547–556.

53 Y. Huang, X. Zeng, L. Guo, J. Lan, L. Zhang and D. Cao, Heavy metal ion removal of wastewater by zeolite-imidazolate frameworks, *Sep. Purif. Technol.*, 2018, **194**, 462–469.

54 E. E. Jasper, V. O. Ajibola and J. C. Onwuka, Nonlinear regression analysis of the sorption of crystal violet and methylene blue from aqueous solutions onto an agro-waste derived activated carbon, *Appl. Water Sci.*, 2020, **10**(6), 1–11.

55 F. Dawodu, G. Akpomie and M. Abuh, Equilibrium Isotherm Studies on the Batch Sorption of Copper (II) ions from Aqueous Solution unto Nsu Clay, *Int. J. Sci. Eng. Res.*, 2012, **3**(12), 1–7.

56 X. Yang, J. Wang, A. M. El-Sherbeeny, A. A. AlHammadi, W. H. Park and M. R. Abukhadra, Insight into the adsorption and oxidation activity of a ZnO/piezoelectric quartz core-shell for enhanced decontamination of ibuprofen: steric, energetic, and oxidation studies, *Chem. Eng. J.*, 2022, **431**, 134312.

57 L. Sellaoui, H. Guedidi, L. Reinert, S. Knani, L. Duclaux and A. B. Lamine, Experimental and theoretical studies of adsorption of ibuprofen on raw and two chemically modified activated carbons: new physicochemical interpretations, *RSC Adv.*, 2016, **6**(15), 12363–12373.

58 R. A. Ali, M. Mobarak, A. M. Badawy, E. C. Lima, M. K. Seliem and H. S. Ramadan, New insights into the surface oxidation role in enhancing Congo red dye uptake by Egyptian ilmenite ore: experiments and physicochemical interpretations, *Surf. Interface*, 2021, **26**, 101316.

59 M. T. Ashraf, A. A. AlHammadi, A. M. El-Sherbeeny, S. Alhammadi, W. Al Zoubi, Y. G. K. Supervison and M. R. Abukhadra, Synthesis of cellulose fibers/Zeolite-A nanocomposite as an environmental adsorbent for organic and inorganic selenium ions; characterization and advanced equilibrium studies, *J. Mol. Liq.*, 2022, **360**, 119573.

60 M. R. Abukhadra, N. M. Refay, A. M. El-Sherbeeny and M. A. El-Meligy, Insight into the loading and release properties of MCM-48/biopolymer composites as carriers for 5-fluorouracil: equilibrium modeling and pharmacokinetic studies, *ACS Omega*, 2020, **5**(20), 11745–11755.

61 K. AbouAitah, M. Bil, E. Pietrzykowska, U. Szałaj, D. Fudala, B. Woźniak, J. Nasiłowska, A. Swiderska-Sroda, M. Lojkowski, B. Sokołowska and W. Swieszkowski, Drug-Releasing Antibacterial Coating Made from Nano-Hydroxyapatite Using the Sonocoating Method, *Nanomaterials*, 2021, **11**(7), 1690.

62 J. Wang, N. Cai, V. Chan, H. Zeng, H. Shi, Y. Xue and F. Yu, Antimicrobial hydroxyapatite reinforced-polyelectrolyte complex nanofibers with long-term controlled release activity for potential wound dressing application, *Colloids Surf., A*, 2021, **624**, 126722.

63 M. Mostafa, M. A. El-Meligy, M. Sharaf, A. T. Soliman and M. R. AbuKhadra, Insight into chitosan/zeolite-A nanocomposite as an advanced carrier for levofloxacin and its anti-inflammatory properties; loading, release, and anti-inflammatory studies, *Int. J. Biol. Macromol.*, 2021, **179**, 206–216.

64 D. Tan, P. Yuan, F. Dong, H. He, S. Sun and Z. Liu, Selective loading of 5-fluorouracil in the interlayer space of methoxy-modified kaolinite for controlled release, *Appl. Clay Sci.*, 2018, **159**, 102–106.

65 F. Rehman, K. Ahmed, A. Rahim, N. Muhammad, S. Tariq, U. Azhar, A. J. Khan, Z. Sama, P. L. Volpe and C. Airoldi, Organo-bridged silsesquioxane incorporated mesoporous silica as a carrier for the controlled delivery of ibuprofen and fluorouracil, *J. Mol. Liq.*, 2018, **258**, 319–326.

66 M. Ge, W. Tang, M. Du, G. Liang, G. Hu and S. J. Alam, Research on 5-fluorouracil as a drug carrier materials with its in vitro release properties on organic modified magadiite, *Eur. J. Pharm. Sci.*, 2019, **130**, 44–53.

67 S. M. Ibrahim, M. N. Bin Jumah, S. I. Othman, R. S. Alruhaimi, N. Al-Khalawi, Y. F. Salama, A. A. Allam and M. R. Abukhadra, Synthesis of Chitosan/Diatomite Composite as an Advanced Delivery System for Ibuprofen Drug; Equilibrium Studies and the Release Profile, *ACS Omega*, 2021, **6**(20), 13406–13416.

68 H. El-Hamshary, M. H. El-Newehy, M. Moydeen Abdulhameed, A. ElFaham and A. S. Elsherbiny, Evaluation of clay-ionene nanocomposite carriers for controlled drug delivery: synthesis, in vitro drug release, and kinetics, *Mater. Chem. Phys.*, 2019, **225**, 122–132.

69 B. Sever, M. D. Altıntop, Y. Demir, G. A. Çiftçi, S. Beydemir and A. Özdemir, Design, synthesis, in vitro and in silico

investigation of aldose reductase inhibitory effects of new thiazole-based compounds, *Bioorg. Chem.*, 2020, **102**, 104110.

70 M. Betsiou, G. Bantsis, I. Zoi and C. Sikalidis, Adsorption and release of gemcitabine hydrochloride and oxaliplatin by hydroxyapatite, *Ceram. Int.*, 2012, **38**(4), 2719–2724.

71 N. Altoom, M. T. Ashraf, S. M. Ibrahim, S. I. Othman, A. A. Allam, H. A. Alqhtani and M. R. Abukhadra, Insight into the loading, release, and anticancer properties of cellulose/zeolite-A as an enhanced delivery structure for oxaliplatin chemotherapy; characterization and mechanism, *J. Sol-Gel Sci. Technol.*, 2022, **103**(3), 752–765.

72 H. E. Alfassam, M. T. Al Othman, M. A. Al-Waili, A. A. Allam and M. R. Abukhadra, Characterization of β-cyclodextrin Hybridized Diatomite as Potential Delivery Systems of Oxaliplatin and 5-Fluorouracil Drugs; Equilibrium Modeling of Loading and Release Kinetics, *J. Macromol. Sci., Part B: Phys.*, 2023, **62**(9), 478–503.